nanomaterials

Article

Hierarchically Developed $Ni(OH)_2@MgCo_2O_4$ Nanosheet Composites for Boosting Supercapacitor Performance

Hammad Mueen Arbi [1,†], Ganesh Koyyada [2,†], Yedluri Anil Kumar [3,4], Dasha Kumar Kulurumotlakatla [5], Jae Hong Kim [2], Md Moniruzzaman [6,*], Salem Alzahmi [3,4,*] and Ihab M. Obaidat [1,4,*]

1 Department of Physics, United Arab Emirates University, Al Ain P.O. Box 15551, United Arab Emirates
2 Department of Chemical Engineering, Yeungnam University, 214-1, Daehak-ro 280, Gyeongsan 712-749, Republic of Korea
3 Department of Chemical & Petroleum Engineering, United Arab Emirates University, Al Ain P.O. Box 15551, United Arab Emirates
4 National Water and Energy Center, United Arab Emirates University, Al Ain P.O. Box 15551, United Arab Emirates
5 Graduate School of Convergence Science, Pusan Nationfivel University, San 30 Jangjeon-dong, Geumjeong-gu, Busan 609-735, Republic of Korea
6 Department of Chemical and Biological Engineering, Gachon University, 1342 Seongnam-daero, Seongnam-si 13120, Republic of Korea
* Correspondence: mani57chem@gachon.ac.kr (M.M.); s.alzahmi@uaeu.ac.ae (S.A.); iobaidat@uaeu.ac.ae (I.M.O.)
† These authors contributed equally to this work.

Abstract: $MgCo_2O_4$ nanomaterial is thought to be a promising candidate for renewable energy storage and conversions. Nevertheless, the poor stability performances and small specific areas of transition-metal oxides remain a challenge for supercapacitor (SC) device applications. In this study, sheet-like $Ni(OH)_2@MgCo_2O_4$ composites were hierarchically developed on nickel foam (NF) using the facile hydrothermal process with calcination technology, under carbonization reactions. The combination of the carbon–amorphous layer and porous $Ni(OH)_2$ nanoparticles was anticipated to enhance the stability performances and energy kinetics. The $Ni(OH)_2@MgCo_2O_4$ nanosheet composite achieved a superior specific capacitance of 1287 F g^{-1} at a current value of 1 A g^{-1}, which is higher than that of pure $Ni(OH)_2$ nanoparticles and $MgCo_2O_4$ nanoflake samples. At a current density of 5 A g^{-1}, the $Ni(OH)_2@MgCo_2O_4$ nanosheet composite delivered an outstanding cycling stability of 85.6%, which it retained over 3500 long cycles with an excellent rate of capacity of 74.5% at 20 A g^{-1}. These outcomes indicate that such a $Ni(OH)_2@MgCo_2O_4$ nanosheet composite is a good contender as a novel battery-type electrode material for high-performance SCs.

Keywords: hybrid structure; $Ni(OH)_2@MgCo_2O_4$ composites; electrode; supercapacitors; battery-type; high performance

check for updates

Citation: Arbi, H.M.; Koyyada, G.; Anil Kumar, Y.; Kumar Kulurumotlakatla, D.; Kim, J.H.; Moniruzzaman, M.; Alzahmi, S.; Obaidat, I.M. Hierarchically Developed $Ni(OH)_2@MgCo_2O_4$ Nanosheet Composites for Boosting Supercapacitor Performance. *Nanomaterials* **2023**, *13*, 1414. https://doi.org/10.3390/nano13081414

Academic Editor: Jipeng Cheng

Received: 17 March 2023
Revised: 10 April 2023
Accepted: 13 April 2023
Published: 19 April 2023

1. Introduction

With the increasing demand for future-generation renewable energy storage cells, supercapacitors (SCs) are holding on as one of the most favored electrochemical devices, due to their ability to provide greater charge/discharge rates, prolonged cycling life, and superior power densities [1–3]. Nevertheless, most SCs are limited by lower energy densities that significantly hamper their further application. As established by the equation ($E = 1/2CV^2$), work voltage and electrode samples have pivotal roles in determining the energy density [4]. In order to attain greater energy densities, a hybrid SC setup could be designed to increased work voltages [5,6]. SCs possess a battery-type faradaic sample as the energy key and a capacitor nanomaterial as the power initiator [7]. Moreover, constructing unique electrodes to achieve greater specific capacities has been contemplated as a way to enhance energy densities [8,9]. Thus, there is a strong desire to develop unique electrode samples with superior electrochemical activities.

Transition-metal oxides, metal hydroxides, and polymer-based conductors have been extensively utilized as superior electrodes owing to their greater specific theoretical capacities [10,11]. Binary-transition-metal oxides (BTMOs) have gained significant attention as unique sample materials because of their varied oxidation states, cheap prices, and simple preparations, in addition to being eco-friendly. Cobalt-type spinel BTMOs that include $CoMnO_4$ [12], $MnCo_2O_4$ [13], $CuCo_2O_4$ [14], and $MgCo_2O_4$ [15] are being investigated as possible SCs. Because of their excellent theoretical capacitance and sufficient reserves of innate magnesium $MgCo_2O_4$ composites have been considered for SCs and Li-ion batteries [16]. Nevertheless, in practical devices, $MgCo_2O_4$ electrodes alone hardly exhibit a superior theoretical capacity (~3120 F/g) due to their simple nanostructure, small surface region, and weak conductivities [17,18]. To enhance the performance limit of $MgCo_2O_4$ electrodes, it is imperative that a rational and unique design be constructed to improve the energy storage properties of $MgCo_2O_4$-type SCs [19,20].

On other hand, nickel hydroxide $Ni(OH)_2$ has been the object of much consideration because of its superior theoretical capacities, superior electrochemical activities, and cheap price [21]. The unique $Ni(OH)_2$ nanoparticle that develops on the electrode interface would extend the specific area with the electrolytes and condense the ion diffusion routes to optimize its energy-storing performance [22–24]. Meng et al. prepared a $ZnCo_2S_4/Ni(OH)_2$ sample with a great capacitance of 2156 F g^{-1} at 1 A g^{-1} and solid stability performances (94.3% retained over 3000 cycles) [25]. Liu et al. prepared MnCo-LDHs@$Ni(OH)_2$ via an easier two-step hydrothermal route that provided a specific capacitance of 2320 F g^{-1} at 3 A g^{-1} [26]. Therefore, the design of $Ni(OH)_2$ sheets and $MgCo_2O_4$ nanoflakes is anticipated to effectively enhance the energy storage activities and impart significant capacities. Meanwhile, it has been shown that electrode materials covered by an amorphous carbon layer display improved stability performances and increased structural stabilities [27–29].

To explore extremely effective, unique, and reliable electrode samples, both $Ni(OH)_2$ particles and $MgCo_2O_4$ nanoflakes were combined to form a $Ni(OH)_2$@$MgCo_2O_4$ nanosheet composite structure. In this study, the novel structure of the $Ni(OH)_2$@$MgCo_2O_4$ nanosheet was engineered and developed via a hydrothermal process. This recently discovered $Ni(OH)_2$@$MgCo_2O_4$ nanosheet composite displayed a specific capacitance of 1287 F g^{-1} at a current density of 1 A g^{-1}, which is superior to that of the $MgCo_2O_4$ nanoflakes and $Ni(OH)_2$ particles alone. Additionally, the $Ni(OH)_2$@$MgCo_2O_4$ nanosheet composite showed a notable cyclic stability of 85.6% over 3500 long cycles. These results demonstrate that the $Ni(OH)_2$@$MgCo_2O_4$ nanosheet composite is a potential electrode material candidate for high-performance SCs.

2. Experimental Section

2.1. Synthesis of $MgCo_2O_4$ Nanoflakes Grown on Ni Foam

$MgCo_2O_4$ nanoflakes were prepared using a hydrothermal method. NF (2×4 cm^{-2}) pieces were handled with ultrasonication to detach oxide impurities on their interface. Clear solutions were optimized through fully dissolving 0.964 g of $Co(NO_3)_2 \cdot 6H_2O$, 0.494 g of $Mg(NO_3)_2 \cdot 6H_2O$, 0.45 g of $CO(NH_2)_2$, 0.083 g of NH_4F, in 60 mL of distilled water (DI water). After that, the mixed solution and the reacted NF were moved to a well-sealed 150 mL autoclave and held in an oven at 140 °C for 8 h. Then, the autoclave was cooled down to a normal temperature, and the NF pieces were removed from the precursors, washed 3 times with DI water and ethanol, and then heated at 60 °C for 12 h, accompanied by annealing at 350 °C for 2 h at a rate of 6 °C min^{-1}. Eventually, the products were acquired and denoted as $MgCo_2O_4$ nanoflakes.

2.2. Preparation of $Ni(OH)_2$@$MgCo_2O_4$ Nanosheet Composite

Following a typical procedure, 2 mmol $NiCl_2 \cdot 6H_2O$ and 4 mmol urea were put into 20 mL of DI water and stirred for 30 min to obtain a clear solution. The mixed precursor with pieces of $MgCo_2O_4$ nanoflakes loaded on Ni foam was then moved to a 40 mL autoclave and maintained at 110 °C for 3 h. After being cooled down to a normal temperature, the samples were rinsed with ethanol and DI water several times and dried at 70 °C for 5 h in a vacuum. The mass loading of the $Ni(OH)_2@MgCo_2O_4$ nanosheet composites was 3.7 mg cm^{-2}. For comparison, $Ni(OH)_2$ was fabricated on Ni foams using a similar procedure. The mass loading of the $MgCo_2O_4$ nanoflake electrode and $Ni(OH)_2$ electrode was 3.7 mg cm^{-2} and 1.9 mg cm^{-2}, respectively.

2.3. Measurements and Characterizations

X-ray powder diffraction (XRD, Bruker D8 Advance with Cu Kα radiation) was used to characterize the crystalline phases of the samples. Field emission scanning electron microscopy (FE-SEM, JSM-7800F) was used to study the morphologies. High-resolution transmission electron microscopy (HRTEM, JEM-2100F at 200 kV) was used to study the microstructures and the elemental compositions. Photoelectron X-ray spectroscopy (XPS; ESCCALAB 250Xi, Busan, Republic of Korea) was used to study the chemical valence states and compositions of samples.

2.4. Measurements and Characterizations

All electrochemical measurements were conducted using a 3-electrode configuration in a 3 M KOH aqueous electrolyte. The fabricated samples, a Ag/AgCl electrode, and a platinum wire were utilized as working electrodes, reference electrodes, and counter electrodes, respectively. Galvanostatic charge–discharge (GCD) and cyclic voltammetry (CV) were acquired on a Bio-Logic- SP-150C electrochemical workstation. Electrochemical impedance spectroscopy (EIS) was employed in the frequency width from 0.01 to 100 kHz. The specific capacitance (C_s, F g^{-1}) was calculated from the GCD plots using the following equation [30]:

$$C_S = \frac{I \times \Delta t}{m \times \Delta V} \quad (1)$$

where I (A), Δt (s), and m (g) have their conventional meanings.

3. Results and Discussion

The synthesis procedure of $Ni(OH)_2@MgCo_2O_4$ is demonstrated in Figure 1. Initially, $MgCo_2O_4$ nanoflakes were developed on Ni foam under simple hydrothermal and annealing technologies. After that, $MgCo_2O_4$ nanoflakes were directly engaged as a skeleton to construct $Ni(OH)_2@MgCo_2O_4$ through secondary hydrothermal procedures. As an outcome, $MgCo_2O_4$ nanoflakes gradually dissolved and generated fresh $Ni(OH)_2$, manifesting a uniform sheet-like $Ni(OH)_2@MgCo_2O_4$ composite.

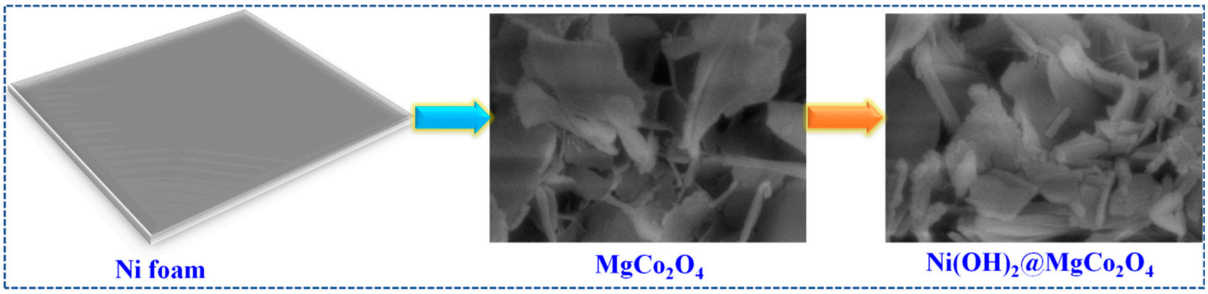

Figure 1. Schematic illustration of the synthesis preparation of $Ni(OH)_2@MgCo_2O_4$ nanosheet composite grown on Ni foam.

The XRD patterns of the $Ni(OH)_2$, $MgCo_2O_4$, and $Ni(OH)_2@MgCo_2O_4$ nanosheet electrodes are displayed in Figure 2. In the XRD tests of $MgCo_2O_4$, except for the diffraction angles from the nickel foam matrixes that remained, long peaks could be clearly identified in the $MgCo_2O_4$ phases [14]. The diffraction peaks positioned at 31°, 36.8°, 44.6°, 58.89°, and 64.98° were attributed to the (2 2 0), (3 1 1), (4 0 0), (4 2 2), and (4 4 0) lattice planes of $MgCo_2O_4$ (JCPDS NO. 02–1073) [12,16,29]. Additionally, three longer peaks were identified at 2θ = 44.5°, 51.85°, and 76.37° that came from the Ni foam skeleton (JCPDS No. 04–0850). Meanwhile, the line angles at 11.4°, 23.7°, and 33.4° were matched to $Ni(OH)_2$ (JCPDS No. 38-0715) [31,32]. In general, the diffraction angles of the $Ni(OH)_2$@$MgCo_2O_4$ nanosheet composite were in good agreement with $Ni(OH)_2$ and $MgCo_2O_4$ [28].

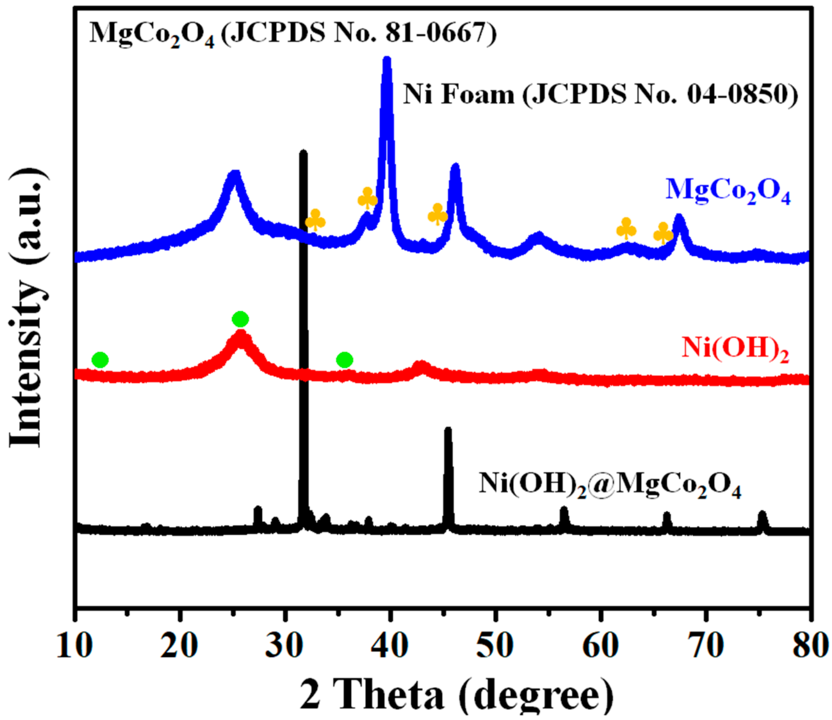

Figure 2. XRD patterns of $Ni(OH)_2$ nanoparticle electrode, $MgCo_2O_4$ nanoflake electrode, and $Ni(OH)_2$@$MgCo_2O_4$ nanosheet composites grown on Ni foam.

XPS was utilized to detect the chemical valence states and compositions of each element in the developed $Ni(OH)_2$@$MgCo_2O_4$ nanosheet composites. Figure 3a depicts the survey spectra, which illustrate the coexistence of Ni, Mg, Co, and O in the composite sample. The Ni 2p XPS spectra are shown in Figure 3b. The angles situated at 873.5 eV in Ni $2p_{1/2}$ and 855.6 eV in Ni $2p_{3/2}$ were ascribed to the Ni^{2+} states, and those located at 876.6 eV in Ni $2p_{1/2}$ and 858.76 eV in Ni $2p_{3/2}$ were attributed to the Ni^{3+} states [33–35]. The straight spectra of Mg 2p seen in the XPS results are shown in Figure 3c, where the peaks in the binding source at 51.2 eV confirm the existence of magnesium oxides. The Co 2p XPS spectra (Figure 3d) possess two spin orbits and two shake-up satellites (denoted as "Sat."). The phases at 794.2 eV and 779.4 eV were attributed to Co^{3+}, whereas the remaining peaks at 798.4 eV and 782.5 eV were ascribed to Co^{2+} [34]. The percentage of oxidation of cobalt ions was calculated based on the fitted peak areas of all the individual peaks in the Co 2p XPS spectra for the $Ni(OH)_2$@$MgCo_2O_4$ nanosheet composites, and was determined to be 41:59 (Co^{2+}:Co^{3+}). As depicted in Figure 3e, the O 1 s XPS spectra are composed of three different peaks labeled as O1, O2, and O3 [36,37]. The O1 peak at 531.2 eV was assigned to metal-oxidized bonds. The O2 peak at 532.8 eV was attributed to the OH^- groups procured from $Ni(OH)_2$. The O3 peak at 535.2 eV was ascribed to the chemisorbed oxidized atoms on the interface. In addition, Figure S1 of XPS full spectra of $MgCo_2O_4$ nanoflakes grown on Ni foam.

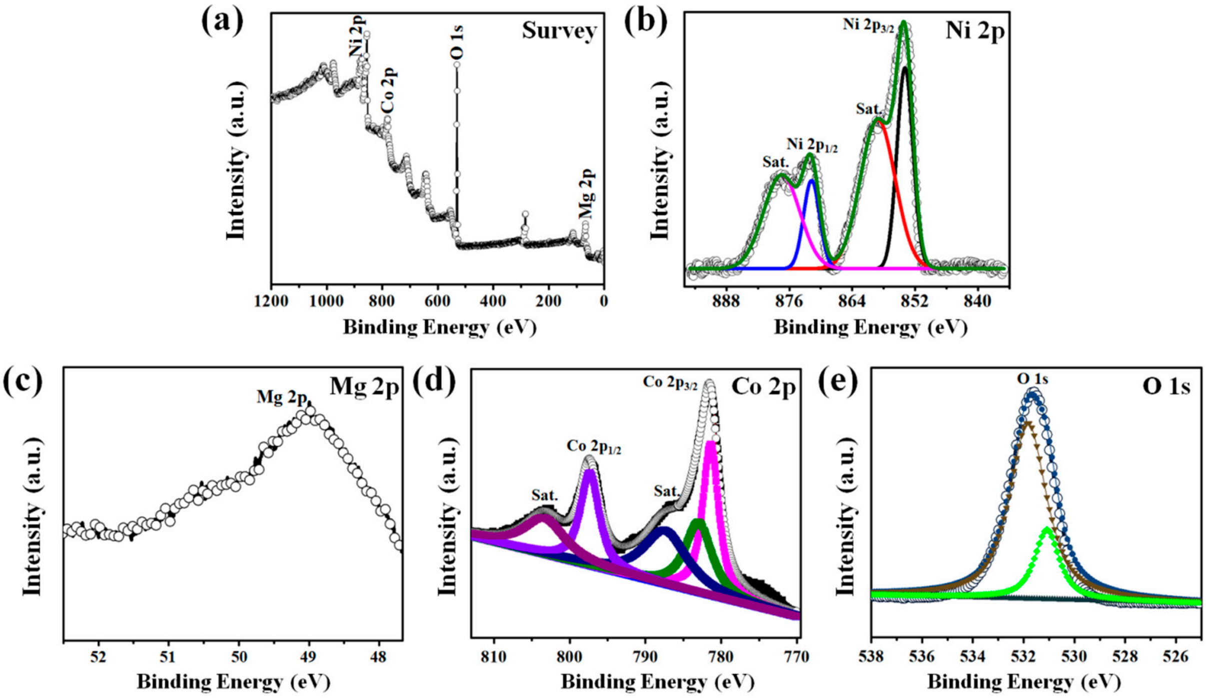

Figure 3. (**a**) XPS full spectra of $Ni(OH)_2@MgCo_2O_4$ nanosheet composite, and high-resolution XPS spectra of $Ni(OH)_2@MgCo_2O_4$ nanosheet composite for (**b**) Ni 2p, (**c**) Mg 2p, (**d**) Co 2p, and (**e**) O 1 s.

The intrinsic nanostructures and morphologies of the $Ni(OH)_2@MgCo_2O_4$ nanosheet composite were analyzed via FE-SEM. The morphological structure of the $MgCo_2O_4$ nanoflake electrode is shown in Figure 4a–c from lower to higher magnifications. Uniform nanoflakes were grown at the edge of the surface, as shown in Figure 4a. Figure 4b,c indicate that the nanoflakes nearly uniformly covered the initial micro-morphology, and their formation was followed by an annealing process. Figure 4d demonstrates that the nanosheets were grown perpendicular to the skeleton. As illustrated in Figure 4e,f, it is obvious that the interface of the $MgCo_2O_4$ nanoflakes was covered with $Ni(OH)_2$ nanoparticles. The buildup of $Ni(OH)_2$ nanoparticles did not demolish the intrinsically ordered nanostructure. The nanoflakes and nanosheets would supply efficient transfer channels for the electrolytes during the charge storage procedures. The $MgCo_2O_4$ nanoflakes were fully positioned on $Ni(OH)_2$ nanoflakes, which favored the effective conductive, preservative furnishing of $MgCo_2O_4$ nanoflakes with ion transportations in the electrolyte, and also provided safe structural stabilities. In addition, the $Ni(OH)_2@MgCo_2O_4$ nanosheet composite supplied abundant active sites for the faradic redox process.

The specific microstructures and morphology of the $MgCo_2O_4$ nanoflakes (Figure 5a) and $Ni(OH)_2@MgCo_2O_4$ nanosheet composite (Figure 5b,c) were obtained using TEM and HRTEM. Figure 5a shows that the $MgCo_2O_4$ nanoflakes existed as the array type, and the nanoflake could be clearly seen. Figure 5b shows the TEM images of a $Ni(OH)_2@MgCo_2O_4$ nanosheet composite, demonstrating $MgCo_2O_4$ has a sheet-type construction with a diameter range of 50 nm [34]. The HRTEM image of the $Ni(OH)_2@MgCo_2O_4$ nanosheet composite illustrates well-defined lattice spacings with interplanar fringes of 0.288 nm and 0.244 nm, which were assigned to the (2 2 0) and (3 1 1) planes of $MgCo_2O_4$ [18,29]. The SAED image (inset in Figure 5c) obtained from the nanosheets reveals their polycrystalline characteristic, which greatly enhances the active sites needed for the Faraday capacity process. As shown in Figure 5d–g, the elements of Ni, Mg, and Co were homogeneously coated in the whole nanosheet, indicating the uniform coexistence of a $Ni(OH)_2@MgCo_2O_4$ nanosheet composite.

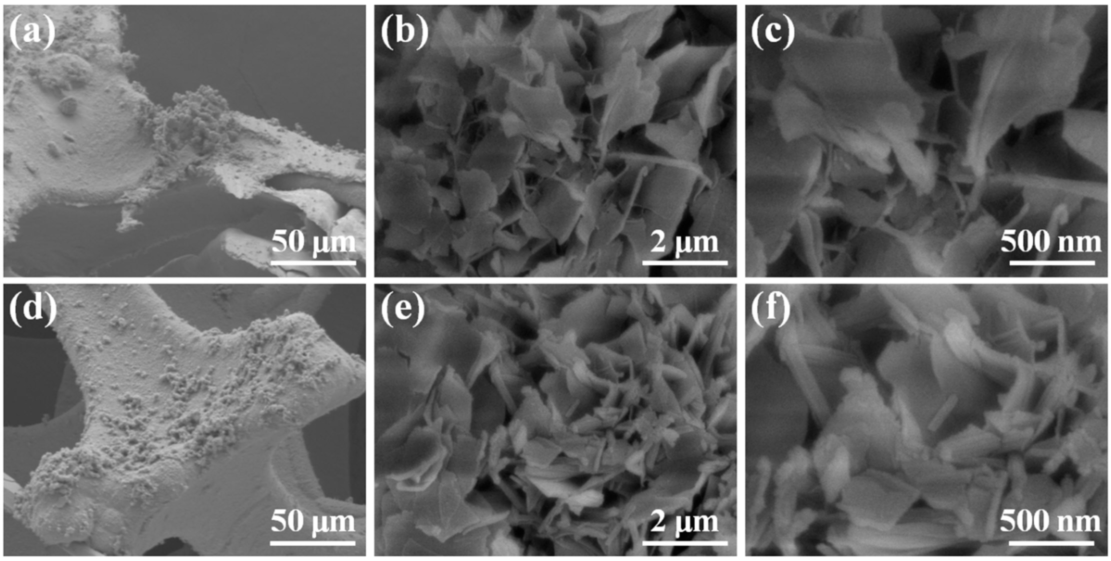

Figure 4. SEM images of the prepared $MgCo_2O_4$ nanoflakes (**a**–**c**) and $Ni(OH)_2@MgCo_2O_4$ nanosheet composite (**d**–**f**).

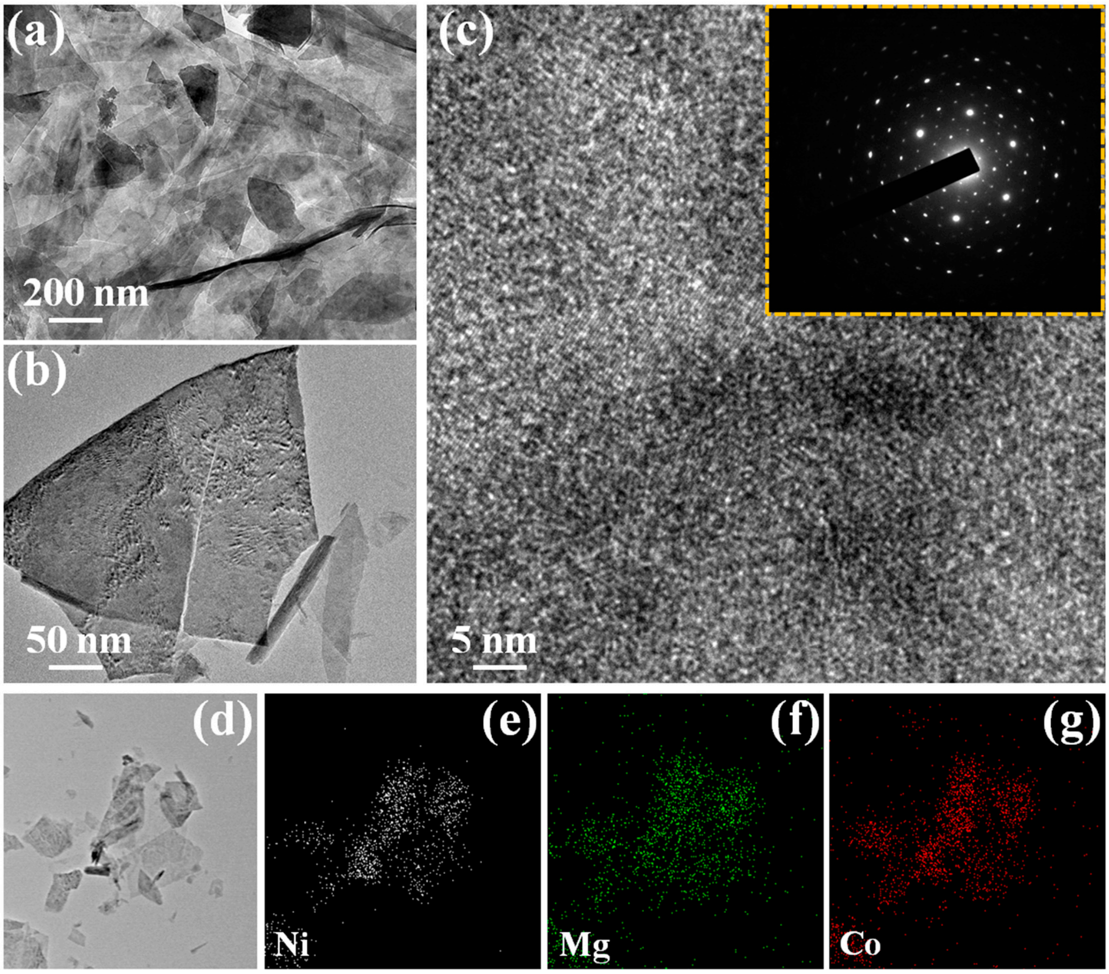

Figure 5. Low-magnification and high-magnification TEM images. (**a**) TEM images of $MgCo_2O_4$ nanoflake electrode; (**b**) TEM images of $Ni(OH)_2@MgCo_2O_4$ nanosheet composite; (**c**) the HRTEM images of the $Ni(OH)_2@MgCo_2O_4$ nanosheet composite (the insets of the selected area show the electron diffraction (SAED) patterns); (**d**–**g**) EDS element mapping images of $Ni(OH)_2@MgCo_2O_4$ nanosheet composite.

Electrochemical Properties of Electrode Materials

To better evaluate the electrochemical behaviors of $Ni(OH)_2$ nanoparticle electrodes, $MgCo_2O_4$ nanoflake electrodes, and $Ni(OH)_2@MgCo_2O_4$ nanosheet composites, CV, GCD, and EIS measurements were conducted using a three-electrode configuration in a 2 M KOH aqueous electrolyte solution (Figure 6). Figure 6a shows the results of the CV tests of as-developed electrodes of the $Ni(OH)_2$ nanoparticle, $MgCo_2O_4$ nanoflake electrodes, and $Ni(OH)_2@MgCo_2O_4$ nanosheet composites at a scanning rate of 5 mV s^{-1}. All electrode samples possessed an obvious couple of reversible redox peaks, demonstrating that active electrodes have typical battery-type characteristics. Particularly, as depicted in the CV test results shown in Figure 6a, the specific area of the $Ni(OH)_2@MgCo_2O_4$ nanosheet composite was much bigger than that of the $Ni(OH)_2$ nanoparticle electrode and $MgCo_2O_4$ nanoflake electrode at similar scan rates, revealing the notable capacitance of $Ni(OH)_2@MgCo_2O_4$ nanosheet composites. Figure 6b depicts the GCD plots of the $Ni(OH)_2$ nanoparticle electrode, $MgCo_2O_4$ nanoflake electrode, and $Ni(OH)_2@MgCo_2O_4$ nanosheet composites at an identical current density of 1 A g^{-1}. Figure 6d,f display the GCD curves of the $Ni(OH)_2@MgCo_2O_4$ nanosheet composite and $MgCo_2O_4$ nanoflake electrodes at different current densities. Based on the GCD tests in Figure 6d,f, the C_s of the $Ni(OH)_2@MgCo_2O_4$ nanosheet composites was measured as 1287 F g^{-1} at 1 A g^{-1}. At higher current density values of 2, 5, 10, and 20 A g^{-1}, the $Ni(OH)_2@MgCo_2O_4$ nanosheet composites also reached good capacitances of 1071, 926, 661, and 459 F g^{-1}, respectively (Figure 6d), which were attributed to the large specific area and excellent ion interlayer exchanges of the composites.

Figure 6c,e display the CV test results for the $MgCo_2O_4$ nanoflake electrode and $Ni(OH)_2@MgCo_2O_4$ nanosheet composites at scanning rates ranging from 5 to 25 mV s^{-1}. The CV tests show that the specific area of the $Ni(OH)_2@MgCo_2O_4$ nanosheet composites was larger, indicating the C_s of the $Ni(OH)_2@MgCo_2O_4$ nanosheet composites was higher.

The specific capacitances of the $Ni(OH)_2@MgCo_2O_4$ nanosheet composites, $MgCo_2O_4$ nanoflake electrodes, and $Ni(OH)_2$ nanoparticle electrodes based on the GCD tests were determined to be 1287 F g^{-1}, 1084 F g^{-1}, and 531 F g^{-1}, respectively, at a current density of 1 A g^{-1} (Figure 7a). Importantly, the $Ni(OH)_2@MgCo_2O_4$ nanosheet composite electrode was found to exhibit notable rate capabilities with 74.5% retention of the starting capacitances at 20 A g^{-1}.

EIS measurements were conducted on the samples, and the corresponding Nyquist plots are presented in Figure 7b. The outline of the impedance spectra possesses three parts. In the high-frequency area, the real axis with intersections reveals the electrolyte's resistances (Rs), including the internal resistance, the interface resistance, and ionic resistance of the electrolytes between the working electrodes and current collector [38]. The semicircle diameters give the charge transfer impedances (Rct) [39]. The line slope in the lower-frequency region is attributed to the Warburg resistance (Rw), which is close to OH^- in the aqueous solution [40,41]. We can see that the $Ni(OH)_2@MgCo_2O_4$ nanosheet composite sample has abundant vertical lines and semicircles with a smaller diameter than those of the $MgCo_2O_4$ nanoflake electrodes and $Ni(OH)_2$ nanoparticle electrodes, indicating rapid electron transportation kinetics and high diffusion ion rates. The EIS outcomes reveal that the $Ni(OH)_2@MgCo_2O_4$ nanosheet composites had lower *R*s (0.59 Ω) and *R*ct (0.07 Ω) compared to the $MgCo_2O_4$ nanoflake electrode (*R*s was 0.81 Ω and *R*ct was 0.36 Ω) and $Ni(OH)_2$ nanoparticle electrode (*R*s was 0.93 Ω and *R*ct was 0.51 Ω), indicating superior electrical conductivities and fast electron transportation kinetics.

Cycling stability is also a crucial factor in studying the characteristics of SCs. Thus, continuous charge/discharge procedures were maintained for $Ni(OH)_2@MgCo_2O_4$ nanosheet composites, $MgCo_2O_4$ nanoflake electrodes, and $Ni(OH)_2$ nanoparticle electrodes at a current density of 2 A g^{-1} over 3500 long cycles. As illustrated in Figure 7c, the $Ni(OH)_2$ nanoparticles and $MgCo_2O_4$ nanoflake electrodes retained 78.3% and 81.2% of their starting capacitances, respectively, over 3500 cycles. However, the hybrid $Ni(OH)_2@MgCo_2O_4$ nanosheet composite electrode (with an initial specific capacitance of 1071 F g^{-1}) retained

85.6% of its initial capacitance after 3500 long cycles. The unique hybrid constructions achieved outstanding cycling stability results. The specific capacitance values of the $Ni(OH)_2$@ $MgCo_2O_4$ electrode were compared with those found in previous studies, as shown in Table 1.

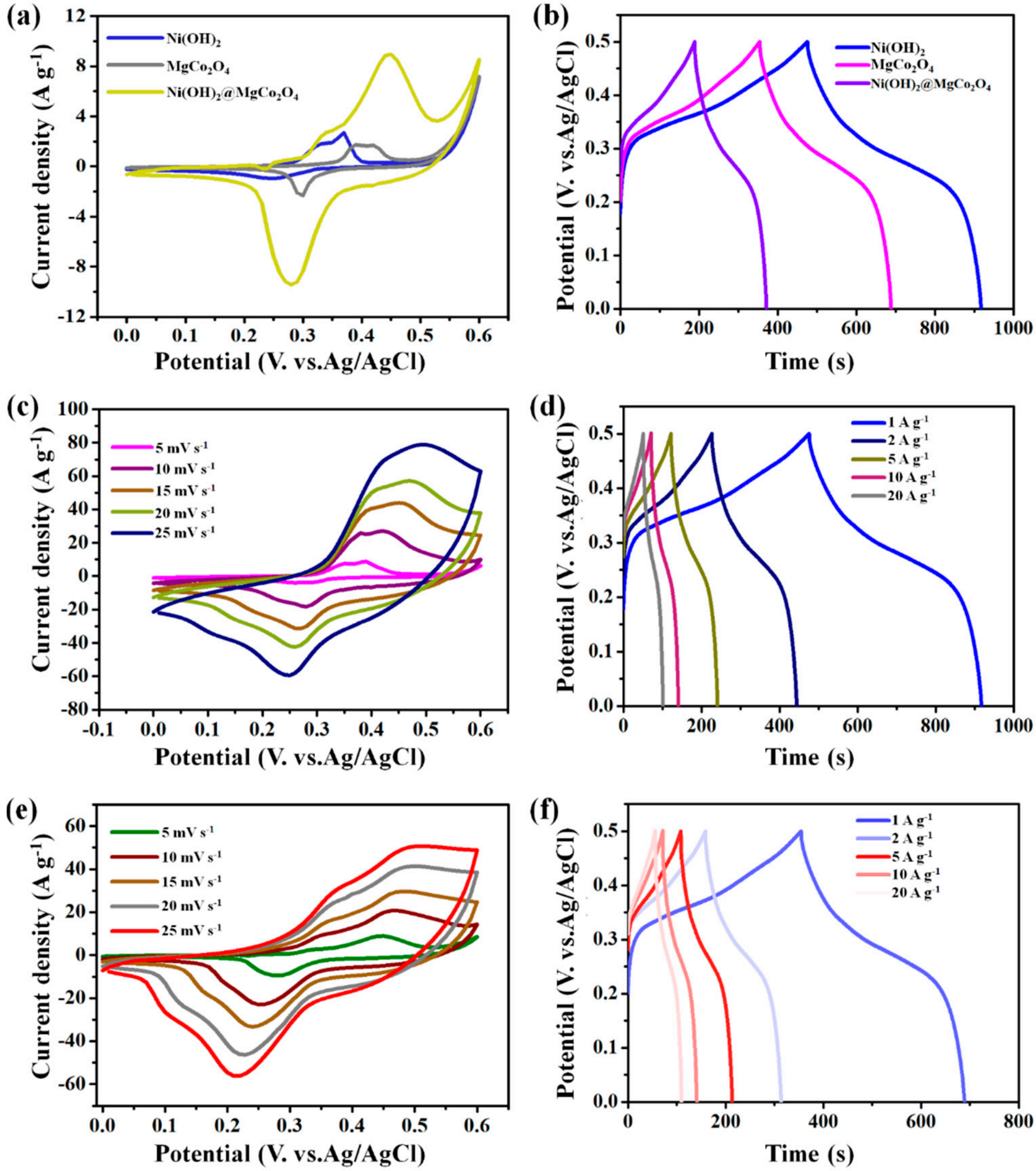

Figure 6. (**a**) Comparison of the CV plots of $Ni(OH)_2$ nanoparticle electrode, $MgCo_2O_4$ nanoflake electrode, and $Ni(OH)_2$@$MgCo_2O_4$ nanosheet composites at a scan rate of 5 mV s^{-1}; (**b**) comparison of the GCD curves of the electrodes at a current density of 1 A g^{-1}; (**c**,**e**) CV curves of the $Ni(OH)_2$@$MgCo_2O_4$ nanosheet composites and $MgCo_2O_4$ nanoflake electrodes at varied scan rates; (**d**,**f**) GCD curves of the $Ni(OH)_2$@$MgCo_2O_4$ nanosheet composite and $MgCo_2O_4$ nanoflake electrodes at different current densities.

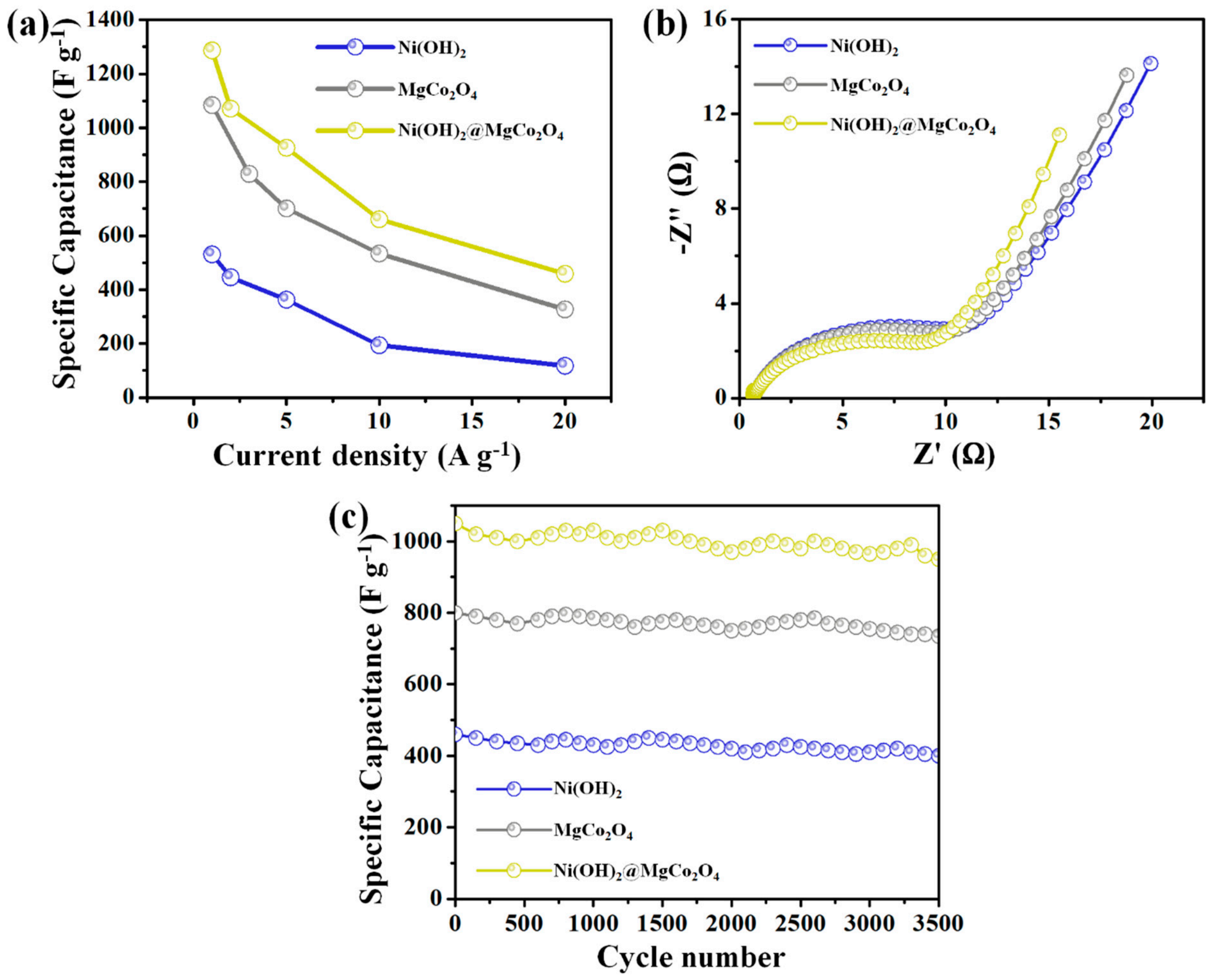

Figure 7. Electrochemical characterization of $Ni(OH)_2$ nanoparticle electrode, $MgCo_2O_4$ nanoflake electrode, and $Ni(OH)_2@MgCo_2O_4$ nanosheet composites: (**a**) specific capacitances of as-developed active electrodes at different current densities; (**b**) Nyquist plots of EIS; (**c**) cycling performance tests over 3500 long cycles at a current density of 2 A g^{-1}.

Table 1. Comparison of electrochemical performance of $Ni(OH)_2$@ $MgCo_2O_4$ electrode with earlier reported studies on a three-electrode system.

Electrode Materials	Electrolyte	Specific Capacitance (F g^{-1})/Current Density	Cycles (Stability)	Ref.
$MgCo_2O_4@MnO_2$	2 M KOH	852.5 F g^{-1} at (1 A g^{-1})	-	[38]
$CeO_2@MnO_2$	1 M Na_2SO_4	255 F g^{-1} at (1 A g^{-1})	3000 (90.1%)	[39]
$MgCo_2O_4$ nanosheets	2 M KOH	947 C g^{-1} (2 A g^{-1})	5000 (96%)	[40]
Double-urchin-like $MgCo_2O_4$	3 M KOH	508 F g^{-1} (2 A g^{-1})	2000 (95.9%)	[41]
1D $MgCo_2O_4$	-	752 F g^{-1} (2 mA cm^{-2})	-	[42]
$MgCo_2O_4$ nanocone arrays	1 M Na_2SO_4	750 F g^{-1} (1 A g^{-1})	1000 (84%)	[43]
Porous $MgCo_2O_4$ nanoneedle	-	804 F g^{-1} (1 A g^{-1})	2000 (87%)	[44]
$MgCo_2O_4$	2 M KOH	321 F g^{-1} (0.5 A g^{-1})	-	[45]
Urchin-like MgCo2O4@PPy	-	1076.9 F g^{-1} (1 A g^{-1})	1000 (97.4%)	[46]
$Ni(OH)_2@MgCo_2O_4$	2 M KOH	1287 F g^{-1} at 1 A g^{-1}	3500 (85.6%)	This work

4. Conclusions

In summary, we successfully fabricated a $Ni(OH)_2@MgCo_2O_4$ nanosheet composite electrode on Ni foam using a facile two-step hydrothermal route followed by annealing techniques. The as-synthesized sample electrodes achieved notable electrochemical activities due to their synergistic effects. Combining the synergistic effects of the outstandingly aligned $MgCo_2O_4$ nanoflakes and unique specific area of $Ni(OH)_2$ nanoparticles, the as-developed $Ni(OH)_2@MgCo_2O_4$ nanosheet composite demonstrated a superior C_s of 1287 F g^{-1} at a current density of 1 A g^{-1} and rate capabilities superior to those of $MgCo_2O_4$ nanoflakes and $Ni(OH)_2$ nanoparticle electrodes alone. Moreover, the $Ni(OH)_2@MgCo_2O_4$ nanosheet composite showed a notable cyclic stability of 85.6% over 3500 long cycles. These features of battery-type electrode materials with outstanding electrochemical performances demonstrate their promise as high-performance SCs.

Supplementary Materials: The following supporting information can be downloaded at: https://www.mdpi.com/article/10.3390/nano13081414/s1, Figure S1: XPS full spectra of $MgCo_2O_4$ nanoflakes grown on Ni foam.

Author Contributions: Conceptualization, I.M.O., Y.A.K. and S.A.; supervision and validation, I.M.O. and S.A.; investigation and writing, H.M.A., Y.A.K., G.K. and D.K.K.; investigation, visualization, and validation, H.M.A., M.M. and J.H.K. All authors have read and agreed to the published version of the manuscript.

Funding: This work was financially supported by the UAEU SUREPLUS Program under grant No. 31S277 and the UAEU Strategic Research Program under grant No. 12R128.

Institutional Review Board Statement: Not applicable.

Informed Consent Statement: Not applicable.

Data Availability Statement: No new data were created or analyzed in this study. Data sharing is not applicable to this article.

Acknowledgments: This work was financially supported by the UAEU SUREPLUS Program under grant No. 31S277 and the UAEU Strategic Research Program under grant No. 12R128.

Conflicts of Interest: The authors declare no conflict of interest.

References

1. Yoon, J.H.; Kumar, Y.A.; Sambasivam, S.; Hira, S.A.; Krishna, T.N.V.; Zeb, K.; Uddin, W.; Kumar, K.D.; Obaidat, I.M.; Kim, S.; et al. Highly efficient copper-cobalt sulfide nano-reeds array with simplistic fabrication strategy for battery-type supercapacitors. *J. Energy Storage* **2020**, *32*, 101988. [CrossRef]
2. Mun, C.H.; Gopi, C.V.V.M.; Vinodh, R.; Sambasivam, S.; Obaidat, I.M.; Kim, H.J. Microflower-like nickel sulfide-lead sulfide hierarchical composites as binder-free electrodes for high-performance supercapacitors. *J. Energy Storage* **2019**, *26*, 100925. [CrossRef]
3. Gopi, C.V.V.M.; Vinodh, R.; Sambasivam, S.; Obaidat, I.M.; Kalla, R.M.N.; Kim, H.J. One-pot synthesis of copper oxide–cobalt oxide core–shell nanocactus-like heterostructures as binder-free electrode materials for high-rate hybrid supercapacitors. *Mater. Today Energy* **2019**, *14*, 100358. [CrossRef]
4. Kumar, Y.A.; Sambasivam, S.; Hira, S.A.; Zeb, K.; Uddin, W.; Krishna, T.N.V.; Kumar, K.D.; Obaidat, I.M.; Kim, H.J. Boosting the energy density of highly efficient flexible hybrid supercapacitors via selective integration of hierarchical nanostructured energy materials. *Electrochim. Acta* **2020**, *364*, 137318. [CrossRef]
5. Bhat, V.S.; Hegde, G.; Nasrollahzadeh, M. A sustainable technique to solve growing energy demand: Porous carbon nanoparticles as electrode materials for high-performance supercapacitors. *J. Appl. Electrochem.* **2020**, *50*, 1243–1255. [CrossRef]
6. Huang, Y.; Zhao, Y.; Bao, J.; Lian, J.; Cheng, M.; Li, H. Lawn-like $FeCo_2S_4$ hollow nanoneedle arrays on flexible carbon nanofiber film as binder-free electrodes for high-performance asymmetric pseudocapacitors. *J. Alloys Compd.* **2019**, *772*, 337–347. [CrossRef]
7. Elshahawy, A.M.; Li, X.; Zhang, H.; Hu, Y.T.; Ho, K.H.; Guan, C.; Wang, J. Controllable $MnCo_2S_4$ nanostructures for high performance hybrid supercapacitors. *J. Mater. Chem. A* **2017**, *5*, 7494–7506. [CrossRef]
8. Sun, W.; Du, Y.; Wu, G.; Gao, G.; Zhu, H.; Shen, J.; Zhang, K.; Cao, G. Constructing metallic zinc–cobalt sulfide hierarchical core–shell nanosheet arrays derived from 2D metal–organic-frameworks for flexible asymmetric supercapacitors with ultrahigh specific capacitance and performance. *J. Mater. Chem. A* **2019**, *7*, 7138–7150. [CrossRef]
9. Yang, Y.; Huang, W.; Li, S.; Ci, L.; Si, P. Surfactant-dependent flower- and grass-like $Zn_{0.76}Co_{0.24}S/Co_3S_4$ for high-performance all-solid-state asymmetric supercapacitors. *J. Mater. Chem. A* **2018**, *6*, 22830–22839. [CrossRef]

10. Li, H.; He, Y.; Dai, Y.; Ren, Y.; Gao, T.; Zhou, G. Bimetallic SnS_2/NiS_2@S-rGO nanocomposite with hierarchical flower-like architecture for superior high rate and ultra-stable half/full sodium-ion batteries. *Chem. Eng. J.* **2022**, *427*, 131784. [CrossRef]
11. Li, Y.; Qian, J.; Zhang, M.; Wang, S.; Wang, Z.; Li, M.; Bai, Y.; An, Q.; Xu, H.; Wu, F.; et al. Co-Construction of Sulfur Vacancies and Heterojunctions in Tungsten Disulfide to Induce Fast Electronic/Ionic Diffusion Kinetics for Sodium-Ion Batteries. *Adv. Mater.* **2020**, *32*, 2005802. [CrossRef] [PubMed]
12. Niu, L.; Wu, T.; Chen, M.; Yang, L.; Yang, J.; Wang, Z.; Kornyshev, A.A.; Jiang, H.; Bi, S.; Feng, G. Conductive Metal-Organic Frameworks for Supercapacitors. *Adv. Mater.* **2022**, *34*, e2200999. [CrossRef] [PubMed]
13. Lee, Y.S.; Kumar, Y.K.; Sambasivam, S.; Hira, S.A.; Zeb, K.; Uddin, W.; Reddy, S.P.R.; Kumar, K.D.; Obaidat, I.M.; Kim, H.J.; et al. $CoCu_2O_4$ nanoflowers architecture as an electrode material for battery type supercapacitor with improved electrochemical performance. *Nano-Struct. Nano-Objects* **2020**, *24*, 100618. [CrossRef]
14. Priya, M.S.; Divya, P.; Rajalakshmi, R. A review status on characterization and electrochemical behaviour of biomass derived carbon materials for energy storage supercapacitors. *Sustain. Chem. Pharm.* **2020**, *16*, 100243. [CrossRef]
15. Chen, X.; Chen, D.; Guao, X.; Wang, R.; Zhang, H. Facile Growth of Caterpillar-like $NiCo_2S_4$ Nanocrystal Arrays on Nickle Foam for High-Performance Supercapacitors. *ACS Appl. Mater. Interfaces* **2017**, *9*, 18774–18781. [CrossRef]
16. Zhou, X.; Yue, X.; Dong, Y.; Zheng, Q.; Lin, D.; Du, X.; Qu, G. Enhancing electrochemical performance of electrode material via combining defect and heterojunction engineering for supercapacitors. *J. Colloid Interface Sci.* **2021**, *599*, 68–78. [CrossRef]
17. Huang, C.; Gao, A.; Yi, F.; Wang, Y.; Shu, D.; Liang, Y.; Zhu, Z.; Ling, J.; Hao, J. Metal organic framework derived hollow NiS@C with S-vacancies to boost high-performance supercapacitors. *Chem. Eng. J.* **2021**, *419*, 129643. [CrossRef]
18. Zhu, Y.; Wu, Z.; Jing, M.; Xuming, J.; Xuming, Y.; Song, W.; Ji, X. Mesoporous $NiCo_2S_4$ nanoparticles as high-performance electrode materials for supercapacitors. *J. Power Source* **2015**, *273*, 584–590. [CrossRef]
19. Arbi, H.M.; Yadav, A.A.; Anil Kumar, Y.; Moniruzzaman, M.; Alzahmi, S.; Obaidat, I.M. Polypyrrole-Assisted Ag Doping Strategy to Boost $Co(OH)_2$ Nanosheets on Ni Foam as a Novel Electrode for High-Performance Hybrid Supercapacitors. *Nanomaterials* **2022**, *12*, 3982. [CrossRef]
20. Moniruzzaman, M.; Anil Kumar, Y.; Pallavolu, M.R.; Arbi, H.M.; Alzahmi, S.; Obaidat, I.M. Two-Dimensional Core-Shell Structure of Cobalt-Doped@MnO_2 Nanosheets Grown on Nickel Foam as a Binder-Free Battery-Type Electrode for Supercapacitor Application. *Nanomaterials* **2022**, *12*, 3187. [CrossRef]
21. Zhang, X.; Wang, Y.; Yu, X.; Tu, J.; Ruan, D.; Qiao, Z.J. High-performance discarded separator-based activated carbon for the application of supercapacitors. *J. Energy Storage* **2021**, *44*, 103378. [CrossRef]
22. Li, J.; Yun, S.; Han, F.; Si, Y.; Arshad, A.; Zhang, Y.; Chidambaram, B.; Zafar, N.; Qiao, X. Biomass-derived carbon boosted catalytic properties of tungsten-based nanohybrids for accelerating the triiodide reduction in dye-sensitized solar cells. *J. Colloid Interface Sci.* **2020**, *578*, 184–194. [CrossRef]
23. Ariharan, A.; Ramesh, K.; Vinayagamoorthi, R.; Rani, M.S.; Viswanathan, B.; Ramaprabhu, S.; Nandhakumar, V. Biomass derived phosphorous containing porous carbon material for hydrogen storage and high-performance supercapacitor applications. *J. Energy Storage* **2021**, *35*, 102185. [CrossRef]
24. Mallesh, D.; Anbarasan, J.; Kumar, P.M.; Upendar, K.; Chandrashekar, P.; Rao, B.V.S.K.; Lingaiah, N. Synthesis, characterization of carbon adsorbents derived from waste biomass and its application to CO2 capture. *Appl. Surf. Sci.* **2020**, *530*, 147226. [CrossRef]
25. Jiang, J.; Zhang, Y.; Nie, P.; Xu, G.; Shi, M.; Wang, J.; Wu, Y.; Fu, R.; Dou, H.; Zhang, X. Progress of nanostructured electrode materials for supercapacitors. *Adv. Sustain. Syst.* **2018**, *2*, 1700110. [CrossRef]
26. Xie, P.; Yuan, W.; Liu, X.; Peng, Y.; Yin, Y.; Li, Y.; Wu, Z. Multifunctional surfactants for synthesizing high-performance energy storage materials. *Energy Storage Mater.* **2021**, *36*, 56–76. [CrossRef]
27. Lobato, B.; Suárez, L.; Guardia, L.; Centeno, T.A. Capacitance and surface of carbons in supercapacitors. *Carbon* **2017**, *122*, 434–445. [CrossRef]
28. Sharma, K.; Arora, A.; Tripathi, S.; Storage, J.E. Review of supercapacitors: Materials and devices. *J. Energy Storage* **2019**, *21*, 801–825.
29. Lin, L.; Liu, J.; Liu, T.; Hao, J.; Ji, K.; Sun, R.; Zeng, W.; Wang, Z. Growth-controlled $NiCo_2S_4$ nanosheet arrays with self-decorated nanoneedles for high-performance pseudocapacitors. *J. Mater. Chem. A* **2015**, *3*, 17652–17658. [CrossRef]
30. Wan, H.; Jiang, J.; Yu, J.; Xu, K.; Miao, L.; Zhang, L.; Chen, H.; Ruan, Y. $NiCo_2S_4$ porous nanotubes synthesis via sacrificial templates: High-performance electrode materials of supercapacitors. *CrystEngComm* **2013**, *15*, 7649–7651. [CrossRef]
31. Wang, H.; Ren, Q.; Brett, D.J.L.; He, G.; Wang, R.; Key, J.; Ji, S. Double-shelled tremella-like NiO@Co_3O_4@MnO_2 as a high-performance cathode material for alkaline supercapacitors. *J. Power Source* **2017**, *343*, 76–82. [CrossRef]
32. Zeng, Z.; Wang, D.; Zhu, J.; Xiao, F.; Li, Y.; Zhu, X. $NiCo_2S_4$ nanoparticles//activated balsam pear pulp for asymmetric hybrid capacitors. *CrystEngComm* **2016**, *18*, 2363–2374. [CrossRef]
33. Wang, C.; Wang, J.; Wu, W.; Qian, J.; Song, S.; Yue, Z.J. Feasibility of activated carbon derived from anaerobic digester residues for supercapacitors. *J. Power Source* **2019**, *412*, 683–688. [CrossRef]
34. Ramachandran, T.; Natarajan, S.; Hamed, F. The role of dysprosium levels in the formation of mixed oxidation states within spinel $MnCo_{2-x}Dy_xO_4$ nanocrystalline powders. *J. Electron Spectrosc. Relat. Phenom.* **2020**, *242*, 146952. [CrossRef]
35. Gu, C.; Ge, X.; Wang, X.; Tu, J. Cation–anion double hydrolysis derived layered single metal hydroxide superstructures for boosted supercapacitive energy storage. *J. Mater. Chem. A* **2015**, *3*, 14228–14238. [CrossRef]

36. Chhetri, K.; Tiwari, A.P.; Dahal, B.; Ojha, G.P.; Mukhiya, T.; Lee, M.; Kim, T.; Chae, S.; Muthurasu, A.; Kim, H.Y. A ZIF-8-derived nanoporous carbon nanocomposite wrapped with Co_3O_4-polyaniline as an efficient electrode material for an asymmetric supercapacitor. *J. Electroanal. Chem.* **2020**, *856*, 113670. [CrossRef]
37. Chhetri, K.; Dahal, B.; Mukhiya, T.; Tiwari, A.P.; Muthurasu, A.; Kim, H.Y. Integrated hybrid of graphitic carbon-encapsulated Cu_xO on multilayered mesoporous carbon from copper MOFs and polyaniline for asymmetric supercapacitor and oxygen reduction reactions. *Carbon* **2021**, *179*, 89–99. [CrossRef]
38. Xu, J.; Wang, L. Fabrication of hierarchical core/shell $MgCo_2O_4$@MnO_2 nanowall arrays on Ni-foam as high–rate electrodes for asymmetric supercapacitors. *Sci. Rep.* **2019**, *9*, 12557. [CrossRef]
39. Zhu, S.J.; Jia, J.Q.; Wang, T.; Zhao, D.; Yang, J.; Dong, F.; Shang, Z.G.; Zhang, Y.X. Rational design of octahedron and nanowire CeO_2@MnO_2 core–shell heterostructures with outstanding rate capability for asymmetric supercapacitors†. *Chem. Commun.* **2015**, *51*, 14840–14843. [CrossRef]
40. Vijaykumar, S.; Nagamuthu, S.; Ryu, K.S. In situ preparation of $MgCo_2O_4$ nanosheets on Ni-foam as a binder-free electrode for high performance hybrid supercapacitors. *Dalton Trans.* **2018**, *47*, 6722–6728. [CrossRef] [PubMed]
41. Xu, J.; Wang, L.; Zhang, J.; Qian, J.; Liu, J.; Zhang, Z.; Zhang, H.; Liu, X. Fabrication of porous double-urchin-like $MgCo_2O_4$ hierarchical architectures for high-rate supercapacitors. *J. Alloys Compd.* **2016**, *688*, 933–938. [CrossRef]
42. Silambarasan, M.; Ramesh, P.S.; Geetha, D.; Venkatachalam, V. A report on 1D $MgCo_2O_4$ with enhanced structural, morphological and electrochemical properties. *J. Mater. Sci. Mater. Electron.* **2017**, *28*, 6880–6888. [CrossRef]
43. Cui, L.; Huang, L.; Ji, M.; Wang, Y.; Shi, H.; Zuo, Y.; Kang, S. High-performance $MgCo_2O_4$ nanocone arrays grown on three-dimensional nickel foams: Preparation and application as binder-free electrode for pseudo-supercapacitor. *J. Power Source* **2016**, *333*, 118–124. [CrossRef]
44. Xu, J.; Wang, L.; Sun, Y.; Zhang, J.; Zhang, C.; Zhang, M. Fabrication of porous $MgCo_2O_4$ nanoneedle arrays/Ni foam as an advanced electrode material for asymmetric supercapacitors. *J. Alloys Compd.* **2019**, *779*, 100–107. [CrossRef]
45. Krishnan, S.G.; Reddy, M.V.; Harilal, M.; Vidyadharan, B.; Misnon, I.I.; Rahim, M.H.A.; Ismail, J.; Jose, R. Characterization of $MgCo_2O_4$ as an electrode for high performance supercapacitors. *Electrochim. Acta* **2015**, *161*, 312–321. [CrossRef]
46. Gao, H.; Wang, X.; Wang, G.; Hao, C.; Zhou, S.; Huang, C. An urchin-like $MgCo_2O_4$@PPy core–shell composite grown on Ni foam for a high-performance all-solid-state asymmetric supercapacitor. *Nanoscale* **2018**, *10*, 10190–10202. [CrossRef]